buildings

MDPI

Essay

Damage Evaluation of T-Stub Connected to Hollow Section Column Using Blind Bolts under Tension

Xin Bu [1,2], Shixiang Xiao [3], Zhanjing Wu [1,2], Xiaolu Li [1,2] and Xinwu Wang [1,2,*]

[1] Department of Civil Engineering, Luoyang Institute of Science and Technology, Luoyang 471023, China; bx@lit.edu.cn (X.B.); 200902201808@lit.edu.cn (Z.W.); lixiaolu.even@stu.xjtu.edu.cn (X.L.)
[2] Henan International Joint Laboratory of New Civil Engineering Structures, Luoyang 471023, China
[3] Department of Civil Engineering, Henan Polytechnic University, Jiaozuo 454003, China; 212308010026@home.hpu.edu.cn
* Correspondence: 200900600357@lit.edu.cn

Abstract: The quantitative calculation and evaluation of seismic damage play a crucial role in ensuring structural safety, conducting performance-based structural analysis, and implementing seismic strengthening measures. However, there is limited research on the damage performance of blind-bolted T-stub steel connections used extensively in prefabricated buildings. In this study, the tensile sub model of a blind-bolted T-stub steel connection in a beam–column joint is investigated. The influence of the flange and web thickness of the T-stub connector, as well as the shear-loaded connecting bolts on the web of the T-stub, on the tensile performance of the sub model are considered. Four tensile destructive tests are conducted on a T-stub connector connected to a hollow section column using blind bolts. The experimental results, including failure modes, force–displacement curves, and strain development in the hollow section column and T-stub, are discussed and analyzed in this study. The test results reveal three main failure modes for this tensile substructure: the plastic deformation of the hollow section column, the bending fracture of the T-stub flange, and the fracture of the T-stub web bolt holes due to compression. Furthermore, a ductile damage finite element analysis method is employed to simulate the fracture damage process of the substructure, and the corresponding damage index is calculated using the typical Park–Ang damage model for evaluation, showing good agreement with the damage classification levels specified in FEMA.

Keywords: damage index; T-stub; hollow section steel column; blind bolt; finite element model

Citation: Bu, X.; Xiao, S.; Wu, Z.; Li, X.; Wang, X. Damage Evaluation of T-Stub Connected to Hollow Section Column Using Blind Bolts under Tension. *Buildings* **2023**, *13*, 2603. https://doi.org/10.3390/buildings13102603

Academic Editor: Andreas Lampropoulos

Received: 1 September 2023
Revised: 8 October 2023
Accepted: 12 October 2023
Published: 15 October 2023

1. Introduction

The emergence of blind bolts as an innovative alternative has introduced a new dimension to structural connections. Blind bolts offer the advantage of unilateral installation, thereby reducing the necessity for access to both sides of the connection. This feature proves particularly advantageous when dealing with intricate geometries or retrofitting existing structures. The traditional rectangular steel tube column and H-beam connection joints are primarily connected through welding, exhibiting characteristics of high stiffness and load-bearing capacity [1,2]. These types of joints are commonly simplified as ideal rigid connections [3]. However, investigations into the damage caused by the Northridge earthquake in the United States and the Kobe earthquake in Japan have shown that these welded rigid joints are prone to brittle fracture failures at the beam's upper and lower flange weld locations under the seismic effects [4–6]. On the other hand, semi-rigid joints with bolted connections have exhibited fewer instances of brittle failure [7]. Furthermore, utilizing bolted connections in steel structures allows for the use of prefabricated connections, leading to enhanced efficiency during on-site installation [8,9]. Recently, there has been a gradual adoption of blind bolts as a novel fastening solution for hollow square steel tube (HSST) members [10,11]. This application addresses the limitations of conventional high-strength bolts when used in such connections. The blind bolt, characterized by its one-sided tightening, reliable load-bearing performance, ease of installation, and excellent seismic resistance, offers distinct advantages. These advantages effectively overcome the challenges associated with conventional high-strength bolts in closed-section connections involving hollow square steel tube (HSST) members [12,13].

In the field of structural engineering, the performance and reliability of connections play a pivotal role in ensuring the overall safety and stability of building structures. At present, the design method used for bolted beam–column joints usually adopts the component method recommended in Eurocode 3. This method can be used to analyze the bending moment bearing capacity, initial rotational stiffness, and rotational capacity of steel frame beam–column joints. The component method in Eurocode 3 [14] can reasonably predict the performance of bolted beam–column end plate connections. This approach simplifies the connection into three regions: tension zone, compression zone, and shear zone. The overall behavior of the connection is derived from amalgamating the individual responses of each component. An equivalent T-stub is the most important component in the tension zone of the beam–column joint. The research on the mechanical characteristics of T-stubs has mainly focused on the test, finite element numerical simulation, and classical mechanical analysis. In the research by SWANSON [3], an investigation was carried out on 48 prototypical T-stub steel connections. The study delved into the failure modes of these T-stub connections, considering different flange thicknesses and bolt spacings. The research explored how the flange-prying forces and web plate tensile capacity were influenced by these variations, while also analyzing the mechanisms responsible for energy dissipation within these connections. The utilization of high-strength steel as the material for T-stub connections has been the subject of exploration in several studies [15–17]. In these studies, the differences in the mechanical performance of T-stub connections were examined, taking into consideration Q690 high-strength steel and Q345MPa mild steel. By comparing the experimental results with EC3 design formulas, it was determined that the direct application of EC3 design formulas is not feasible for predicting the yield-bearing capacity of T-stub connections constructed using high-strength steel. The numerical modeling methods for T-stub connections employing stainless steel bolts were explored by YAPICI O [18,19]. The optimal modeling approach was determined, and an analysis was conducted on the mechanical performance of T-stub connections with stainless steel bolstering. Wang [13,20] studied the failure mode of the connections using blind-bolted T-stubs and HSST under tension. Wang also made enhancements to the Gomes model and Yeomans model and proposed a design approach for the tensile yield strength of blind bolt connections. Additionally, the study examined the mechanical behavior of this connection under cyclic loading, analyzing strength degradation, deformation capacity, and stiffness reduction.

It can be observed that although there have been numerous achievements in previous research regarding blind-bolted T-stub connections, the relevant research results on the quantitative calculation and evaluation of the damage to this connection are very limited. The quantitative calculation of damage and seismic damage assessment in beam–column joints are very important for the safety of steel frame structures, performance-based structural analysis, and seismic reinforcement. Therefore, it is highly imperative to investigate the damage and failure patterns of connections using blind-bolted T-stubs and HSST. In this research, the failure process and load–displacement relationship of this kind of connection were studied through experiments. The finite element numerical model of the connection was established, and the fracture simulation of the joints was carried out using the material constitutive model of ductile damage. On the basis of test and finite element analysis, the damage index model was used to calculate the damage of the connections using blind-bolted T-stubs and HSST, and the damage assessment was carried out according to the structural performance level specified by FEMA365.

2. Experimental Investigation

2.1. Test Specimens

Since the thickness of the web and flange of the T-stub, and also the bolts on the connecting web, have a great influence on the connection of HSST to T-stubs connected using blind bolts, four specimens with a ratio of 1:1 were designed in this study and a monotonic tensile load test was conducted on them. The connection studied in this research can be divided into three parts according to the component method, namely the T-stub, the HSST, and the blind bolts, as shown in Figure 1. The specimen IDs and related information are listed in Table 1. The section of HSST is 250 × 250 × 12 with a length of 1.5 m. All T-stubs had a cross-section of 270 mm × 200 mm, thickness of flange, t_f, of 10 mm or 30 mm, and a thickness of web, t_w, of 8 mm or 9 mm, as shown in Figure 2. Blind bolts were used to connect the T-stub to the HSST, and conventional bolts were used to connect the web of the T-stub. All bolts adopted in the test were M20 high-strength bolts conforming to the Class 10.9 catalog, that is, the nominal diameter, d, of the bolts was 20 mm and the nominal yield strength was not lower than 1000 MPa. Blind bolts are nested bolts, with a bolt hole diameter of 30 mm and a bolt hole of 24 mm for connecting the web of the T-stub, as shown in Figure 1.

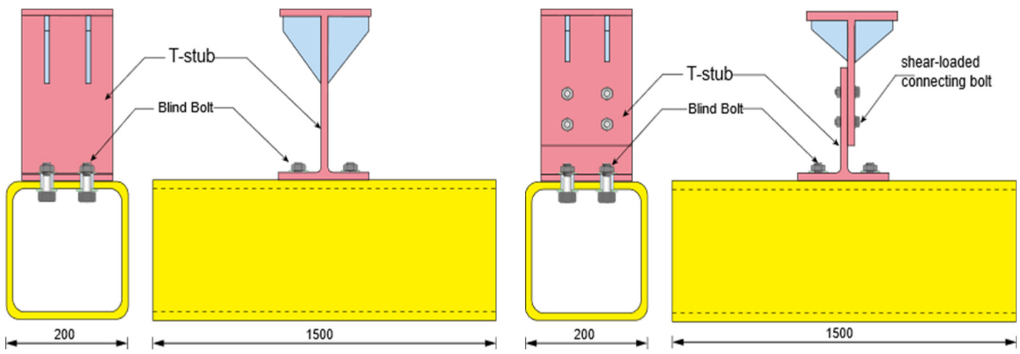

(**a**) TJD-1 and TJD-2 (**b**) TJD-3 and TJD-4

Figure 1. Geometrical parameters of the specimen (unit: mm).

Table 1. Parameters of specimens.

Specimen ID	T-Stub				HSST			Bolt	
	H	**B**	**tw**	**tf**	**Section**	**tc**	**l**	**T-Stub Flange**	**T-Stub Web**
TJD-1	270	200	8	12	250 × 250	12	1200	Blind bolt	-
TJD-2	270	200	9	14	250 × 250	12	1200	Blind bolt	-
TJD-3	270	200	8	12	250 × 250	12	1200	Blind bolt	High-strength bolt
TJD-4	270	200	9	14	250 × 250	12	1200	Blind bolt	High-strength bolt

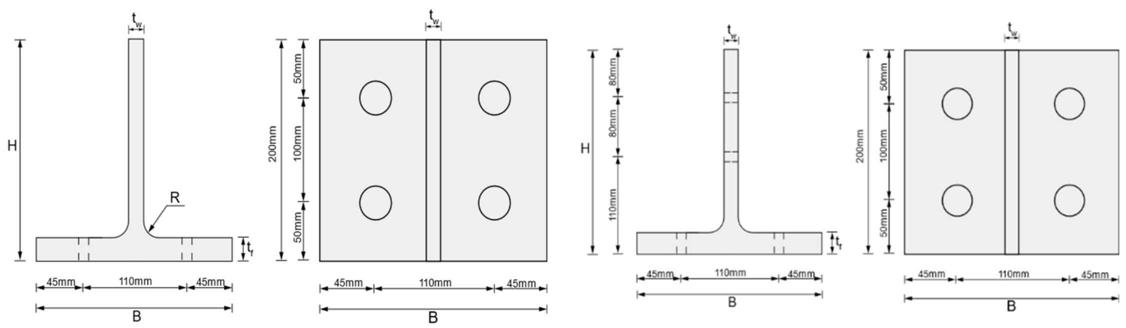

(**a**) TJD-1 and TJD-2 (**b**) TJD-3 and TJD-4

Figure 2. Geometric configuration for T-stub components (unit: mm).

2.2. Material Properties

The steel used in all of the connection specimens, i.e., the HSST, flanges, and webs of the T-stub connectors, came from the same batch of Q235 to make standard metal tensile test specimens. There were five groups of tensile specimens, with 3 specimens in each group, for a total of 15 specimens. The test results are taken as the average value of each group. Table 2 lists the mechanical properties of the steel specimens, where f_y is the yield strength of the steel, f_u is the ultimate strength of the steel, and E is the elastic modulus and elongation. The material characteristics of the bolt were provided by the manufacturer. The yield strength was 950 MPa, the tensile strength was 1060 MPa, the elastic modulus was 210 GPa, the Poisson's ratio was 0.3, and the elongation was 20%.

Table 2. Mechanical properties of steels.

Samples	Sample Thickness/mm	f_y/MPa	f_u/MPa	E/GPa	Elongation/%
HSST	12	283	456	203	30.0
T-stub	12	266	423	201	38.7
flange	14	287	448	198	36.3
T-stub	8	281	453	208	33.5
web	9	313	464	206	32.1

2.3. Test Setup and Instrumentation

The test equipment consists of a rigid reaction frame, an electro-hydraulic servo loading system, and a fixing device. The maximum load of the electro-hydraulic servo actuator is 1000 kN, with a moving stroke of ±250 mm. The test installation scheme is shown in Figure 3, and the test site can be seen in Figure 4. The T-stub was connected to the HSST by blind bolts using a torque wrench with a torque value of 300 N·m. The tensile load applied to the T-stub and the displacement in the vertical direction of the T-stub web were measured during the test. Strain gauges were placed on the web and flange of the T-stub, and also on the wall of the hollow square steel tube. The strain gauge layout is shown in Figure 5. The plastic deformation of the specimen was investigated according to the collected strain data.

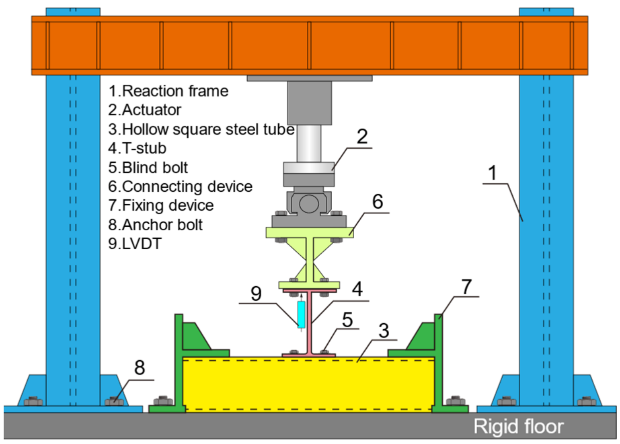

Figure 3. Test installation scheme.

The test was carried out according to two loading steps. The first step was preloading, applying 25 kN of tensile force to the specimen at a loading rate of 5 kN/min. The purpose was to eliminate the gap between the specimen and the installation of the test equipment, and also to check the working state of the strain gauge. It was unloaded when the load reached 25 kN. The second step was formal loading, applying tensile displacement at a rate of 0.5 mm/min. During the test, if it was found that the test specimen was fractured, there was obvious local buckling failure, or the force in the load–displacement curve monitored by the test was less than 85% of the ultimate force, the test was terminated.

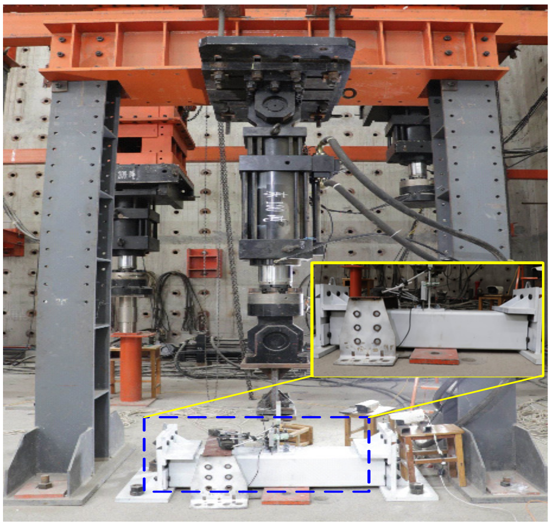

Figure 4. Test setup photograph.

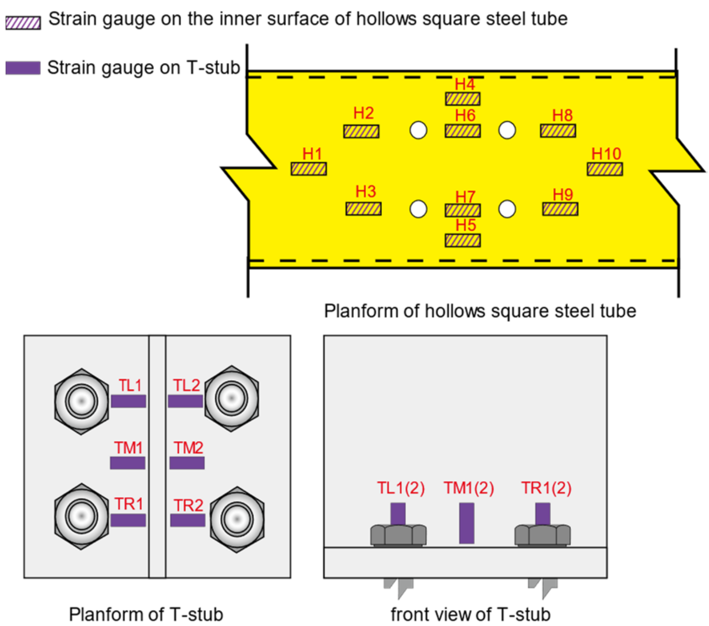

Figure 5. Labels and arrangement of strain gauges on specimen.

3. Test Results

3.1. Failure Mode

3.1.1. HSST Wall Yielding

Figure 6 illustrates the failure mode of the HSST wall, and it can be seen from the figure that the failure modes of the HSST wall all exhibit out-of-plane expansion deformation caused by tension near the bolt hole. TJD-3 and TJD-4 featured T-stubs with bolts subjected to shear forces, resulting in significantly larger out-of-plane deformations in the HSST walls compared to specimens TJD-1 and TJD-2, which were tested without shear-loaded connecting bolts. Moreover, the TJD-3 specimen, in which the flange and web thickness of the T-stub were thinner than the other specimens, had the largest out-of-plane deformation of the HSST wall under the tension state. Similarly, compared to the TJD-1 and TJD-2 specimens without bolts on the web of the T-stub, the out-of-plane deformation of the HSST wall caused by the thinner web and flange thickness of the T-stub connector TJD-1 under tensile force was greater than that of TJD-2.

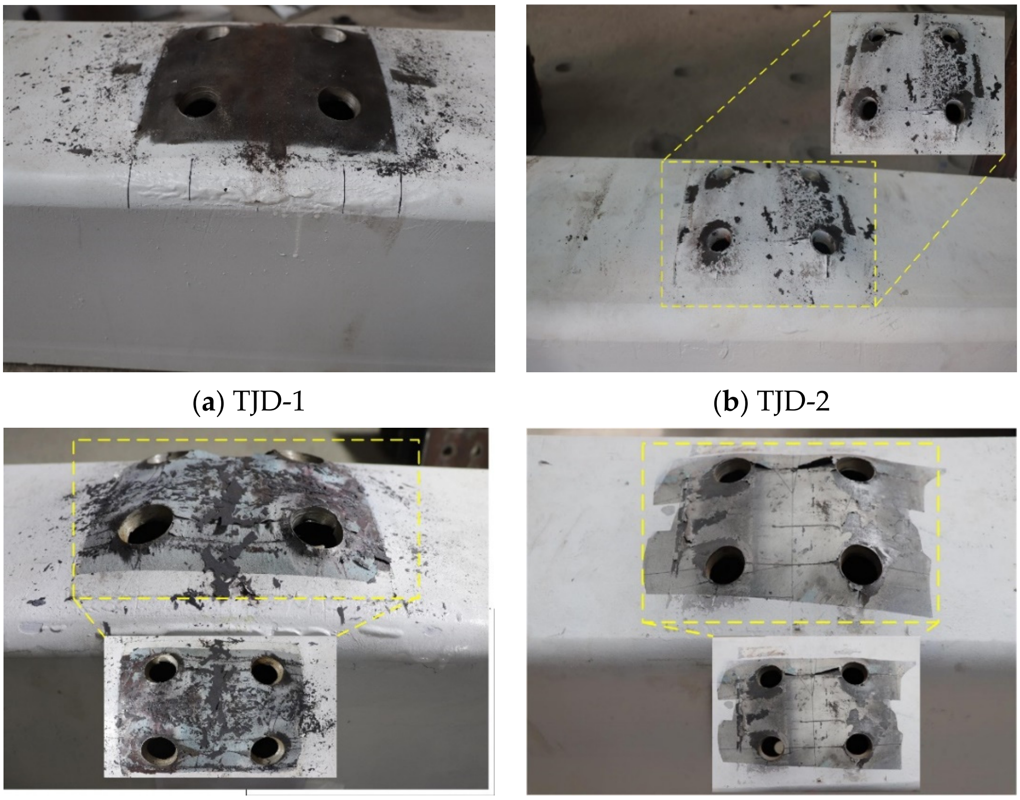

(**a**) TJD-1 (**b**) TJD-2

(**c**) TJD-3 (**d**) TJD-4

Figure 6. Failure mode of the HSST wall.

3.1.2. T-Stub Steel Fracture

As the tensile force reached the yield load, the flanges of all specimens' T-stubs underwent varying degrees of plastic bending deformation. With the continuous increase in the load, the plastic deformation of the flanges of the T-stub intensified, and the flanges became obviously separated from the wall of the HSST. At the ultimate load level, the specimens TJD-1 and TJD-2 exhibited fractures at the junction of the T-stub web and flange, as shown in Figure 7a,b. As shown in Figure 7c, where the web is connected by bolts in specimen TJD-3, the T-stub experienced a complete fracture at the junction of the web and flange. Under ultimate conditions, the T-stub of TJD-4 experienced severe compression deformation at the bolt hole of the web. Consequently, a transverse fracture occurred along the bolt hole, as depicted in Figure 7d.

3.2. Load–Displacement Curves

The load–displacement curves of all test specimens at the joints in all directions are presented in Figure 8. The yield-bearing capacity, yield displacement, initial secant stiffness, ultimate bearing capacity, ultimate displacement, and ductility coefficient of the specimen can be analyzed according to the load–displacement relation curve. In this study, the equivalent elastic–plastic energy method is employed to analyze the force–displacement relationship curve, as illustrated in Figure 9. The peak load, Fmax, is obtained by projecting the extremum point M from the force–displacement relationship curve onto the force coordinate axis. Point D is obtained by projecting the extremum point M onto the displacement coordinate axis. Drawing a line from any point C on the projected segment of the force–displacement relationship curve to the origin point O ensures that the area of the right-angled trapezoid OCMD is equal to the area enclosed by the force–displacement relationship curve in the area of the quadrilateral OAMD, represented as $S_{OCMD} = S_{OAMD}$. Subsequently, a perpendicular line drawn from point C on the displacement axis intersects the curve at point B. The horizontal coordinate value of point B is the yield displacement δ_y, and the vertical coordinate value is the yield-bearing capacity F_y. The vertical coordinate value of point M is the yield-bearing capacity Fu, and the horizontal coordinate value of point N is the ultimate displacement δ_u. The ratio of yield-bearing capacity to yield displacement represents the initial secant stiffness of the curve, while the ratio of the ultimate displacement to yield displacement corresponds to the ductility of the specimen.

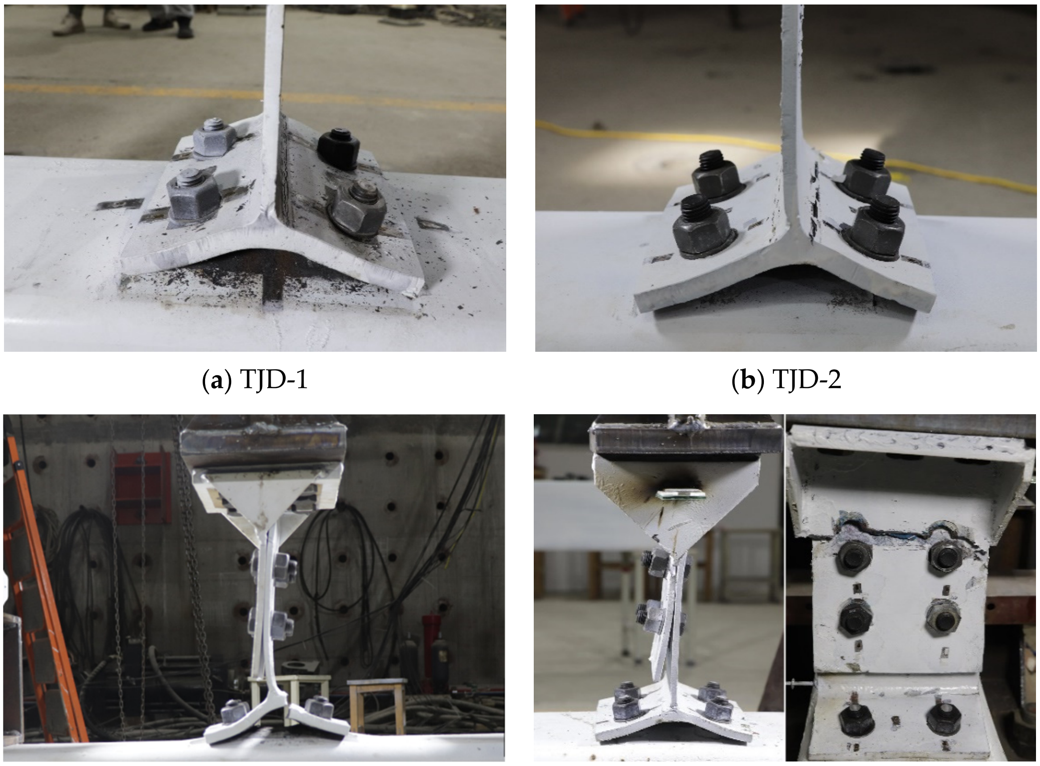

(**a**) TJD-1 (**b**) TJD-2

(**c**) TJD-3 (**d**) TJD-4

Figure 7. Failure mode of T-stubs.

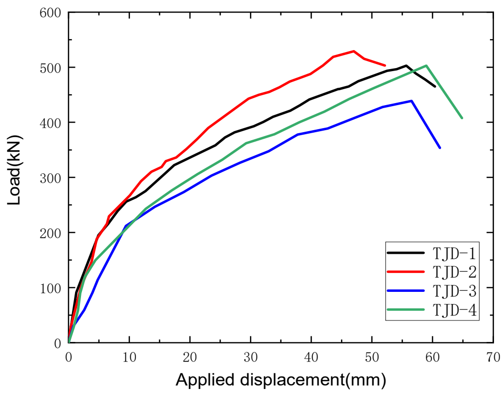

Figure 8. Load–displacement curves.

Based on Figure 5 and Table 3, an analysis of the mechanical characteristics of the joints can be conducted. Compared with TJD-1, the flange thickness of the T-stub is larger, and the yield-bearing capacity of TJD-2 is increased by 20.46% and the ultimate bearing capacity by 5.24% compared to TJD-1. The initial tensile stiffness (***Sc,ini***) of TJD-2 is roughly equivalent to that of TJD-1, and the ductility coefficient (μ) of TJD-1 is 39.77% higher than that of TJD-2. Similarly, the flange thickness of TJD-4's T-stub is larger than that of TJD-3, and the yield-bearing capacity and ultimate bearing capacity of TJD-4 are increased by 14.29% and 14.56% compared with that of TJD-3. The initial tensile stiffness of TJD-3 differs by 3.89% compared with that of TJD-4, and the ductility coefficient of TJD-3 is very close to that of

TJD-4. Through the above analysis, it can be seen that increasing the thickness of the T-stub flange has a significant effect on improving the yield-bearing capacity of the connection, and the initial tensile stiffness of the connection is not significantly affected. Moreover, the relatively thinner thickness of the HSST wall is prone to deformation compared to the other components of the connection, which is the main reason why the initial tensile stiffness of the connection is basically the same. The ductility coefficient of TJD-1 is higher than that of TJD-2, because the T-stub's flange thickness in TJD-1 is thinner; that is, the bending stiffness is lower, and the flange has a large bending deformation after yielding, which increases the ultimate displacement of the connection.

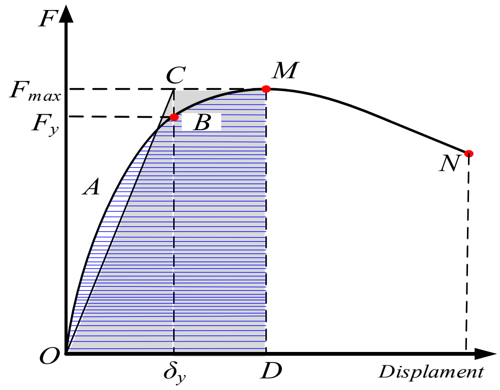

Figure 9. Equivalent elastoplastic energy method.

Table 3. Characteristic values of connection tensile strength and corresponding displacement.

Specimen ID	*Sc,ini*/kN/mm	F_y/kN	δ_y/mm	*Fu*/kN	δ_u/mm	μ
TJD-1	14.64	370.26	25.28	502.74	60.45	2.39
TJD-2	14.67	446.02	30.41	529.08	52.12	1.71
TJD-3	9.77	358.29	36.61	438.95	61.19	1.67
TJD-4	10.15	411.75	40.57	502.85	64.83	1.60

To analyze the influence of the bolted connection form on the mechanical characteristics of the T-stub on the web, the mechanical properties of TJD-1 and TJD-3, as well as TJD-2 and TJD-4, were compared. The yield-bearing capacity of TJD-3 with connecting bolts in the T-stub web decreased by 3.23% compared to TJD-1, the ultimate load decreased by 12.69%, the initial tensile stiffness decreased by 33.27%, and the ductility coefficient decreased by 30.13%. Similarly, comparing TJD-4 and TJD-2, the yield-bearing capacity of TJD-4 decreased by 7.68%, the ultimate load decreased by 4.96%, and the initial tensile stiffness decreased by a maximum of 30.81%. The ductility also decreased by 6.43%. The above analysis indicates that the bolts connected to the T-section web, which are subjected to shear forces, have an obvious influence on the mechanical properties of the connection, and each index has a varying degree of decline.

3.3. Strain Response

H1~H10 strain gauges are arranged on the HSST wall to measure the development of out-of-plane deformation of the HSST wall under tension, as shown in Figure 5. Experimental testing revealed that the deformation of the HSST wall primarily occurs near the bolt holes with larger forces and gradually develops around them. Therefore, based on symmetry, strain gauges (H4, H6, H8) near one of the four bolt holes were selected to analyze the deformation of the HSST wall. Figure 10 illustrates the trend of strain development on the HSST wall. According to the distribution of strain development, the strain (H6) between the two bolt holes along the length direction of the HSST developed the fastest, followed by the strain (H4) at the edge of the column wall, indicating that the deformation develops slowly in the initial stage of loading and rapidly in the later stage of loading. The strain development away from the bolt holes along the length of the HSST gradually diminished.

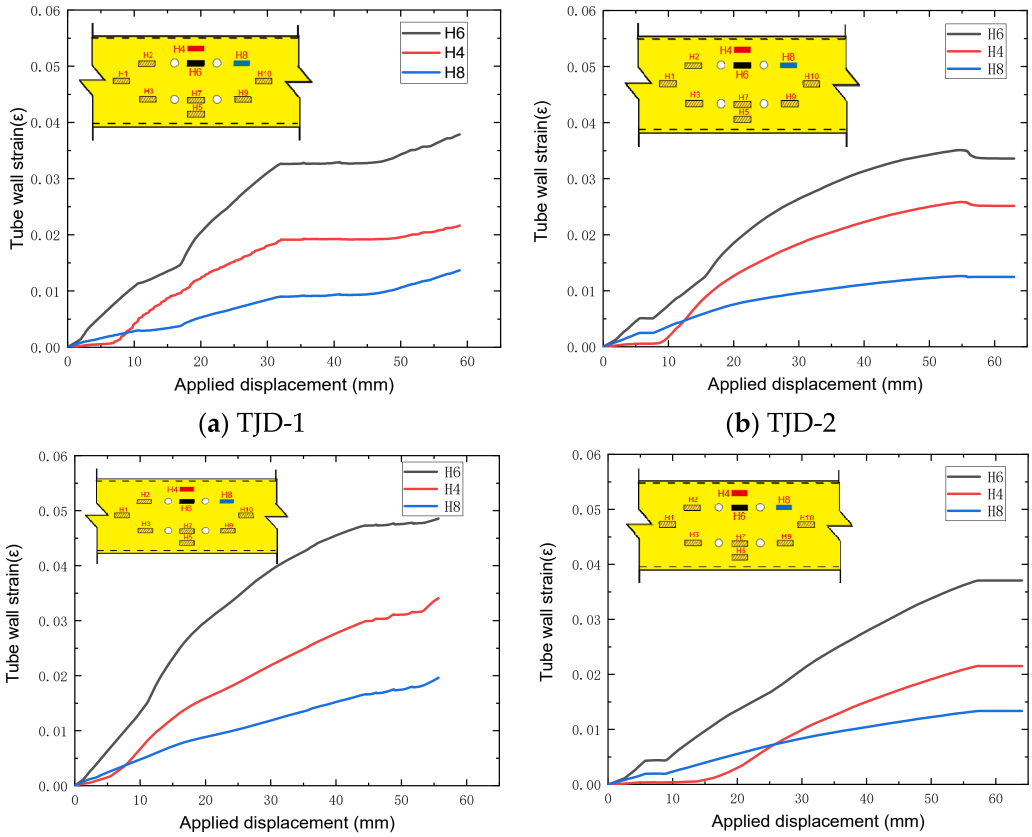

(**a**) TJD-1 (**b**) TJD-2

(**c**) TJD-3 (**d**) TJD-4

Figure 10. Strain development of the HSST tube wall.

Figure 5 illustrates the response at the intersection of the flange and web of the T-stub, where TL1 and TR1 represent the left and right strain gauges near the bolt at the junction of the flange and web, respectively, and TL3 and TR3 represent the left and right strain gauges near the bolt at the junction of the flange and web, respectively. It can be seen from Figure 11 that the strain development on the right side of the junction of the T-stub flange was greater than on the left side. The main reason is that there was a gap between the bolt rod and the sleeve of the blind bolt. Under the action of loads during the initial phase, slight slippage occurred in the bolt rod, leading to uneven stress distribution in the flange of the T-stub, resulting in asymmetric strain development at the junction of the flange and web. As the load continued to increase, the screw, sleeve, and bolt hole wall of the blind bolt came into complete contact, and the strain gradually increased, with the strain value in the middle being greater than that on both sides. When the load was applied to the limit state of TJD-1, TJD-2, and TJD-3, the strains at the right-side junction of the flange and web of the T-stub began to decline after the strain reached approximately 0.3; this is consistent with the failure phenomena of the specimens TJD-1, TJD-2, and TJD-3. Under the ultimate load state, the strain at the junction of the flange and web of the T-stub of TJD-4 remained within the range of 0.04 to 0.06, indicating stable plastic deformation. The main reason is that the thickness of the T-stub flange of TJD-4 was larger, and the thickness of the web was unchanged. As a result, the plastic deformation of the T-stub connection was mainly concentrated at the bolt holes of the web. When the load reached the ultimate state, fractures occurred in the bolt holes of the web, causing the T-stub to be unable to withstand any more pressure. Therefore, the plastic strain at the junction of the web and flange of the T-stub remained stable.

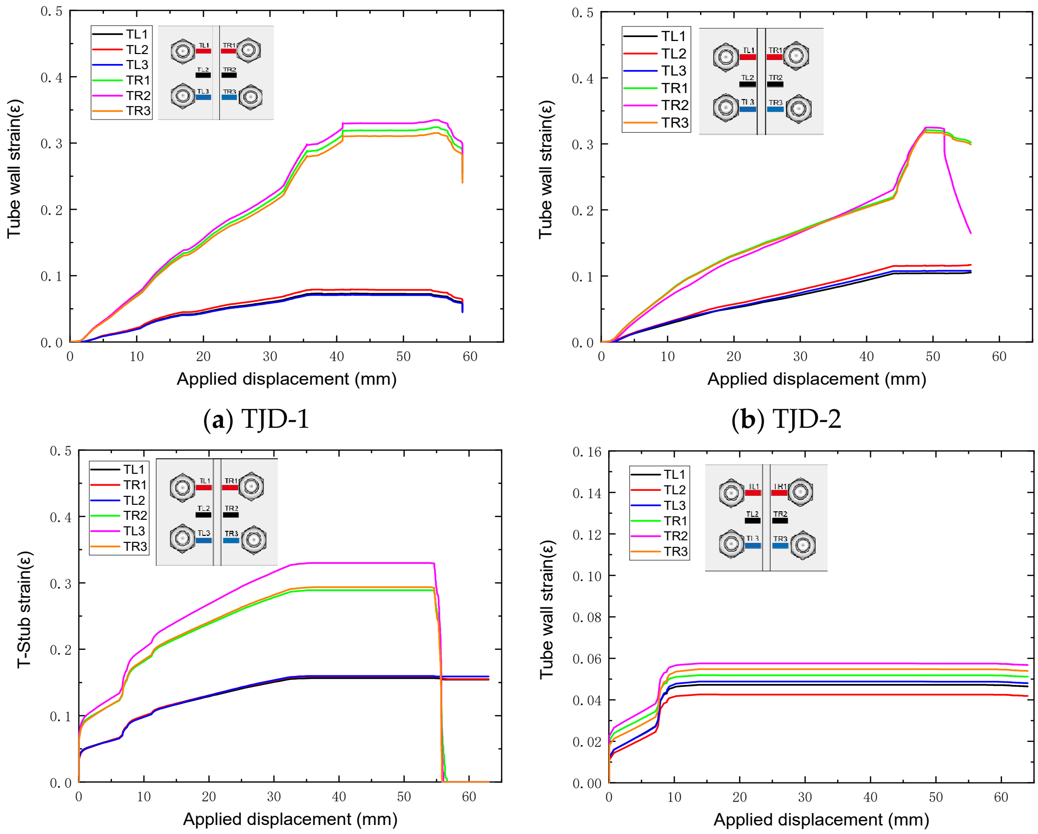

(**a**) TJD-1 (**b**) TJD-2

(**c**) TJD-3 (**d**) TJD-4

Figure 11. Strain development of the T-stub.

4. Finite Element Analysis

4.1. Finite Element Model

In order to comprehensively analyze the mechanical performance of the T-stub connected to the hollow section column using blind bolts under monotonic loads and the overall plastic deformation and failure mechanisms that are not reflected in the experimental research, a nonlinear numerical simulation calculation of the test model was carried out using the ABAQUS2021 software. Considering the symmetry of the model and the time involved in carrying out the finite element calculation, following References [21,22], the finite element model established in this study represents half of the entire structure. Figure 12a shows the finite element models of TJD-1 and TJD-2, and Figure 12b shows the finite element models of TJD-3 and TJD-4. The model included the component HSST, T-stub, high-strength blind bolts, sleeves, and high-strength bolts, and the element type C3D8R was selected. To enhance computational efficiency and convergence, different parts and areas were used in different mesh sizes. The mesh size near the bolts, nuts, bolt rods, washers, T-stubs, and bolt holes was set to 3 mm, and the mesh size of the remaining areas was 9 mm. The contact relationships between all components in the finite element model were defined as normal contact and tangential contact, in which the normal contact adopted hard contact to prevent the penetration of the mesh model, and the tangential contact was set with a friction coefficient of 0.3 [23,24]. The analysis was divided into three steps. The first step was to apply a preload to all bolt cross-sections; the second step was to maintain the deformation length of the bolt rod based on the preload; and the third step was to apply a displacement load on top of the T-stub.

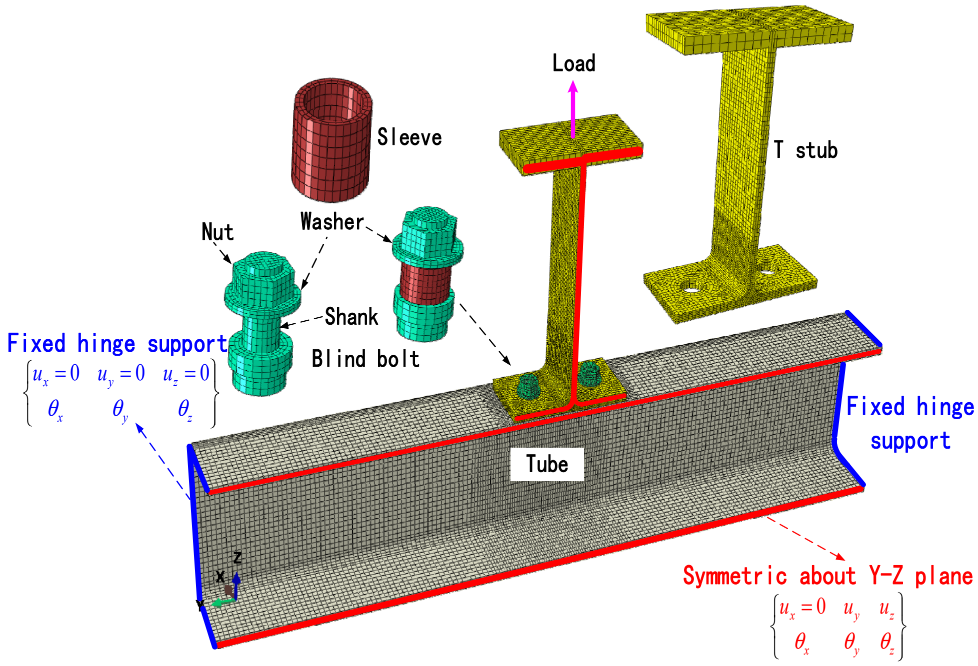

(**a**) Finite element model of TJD-1 and TJD-2

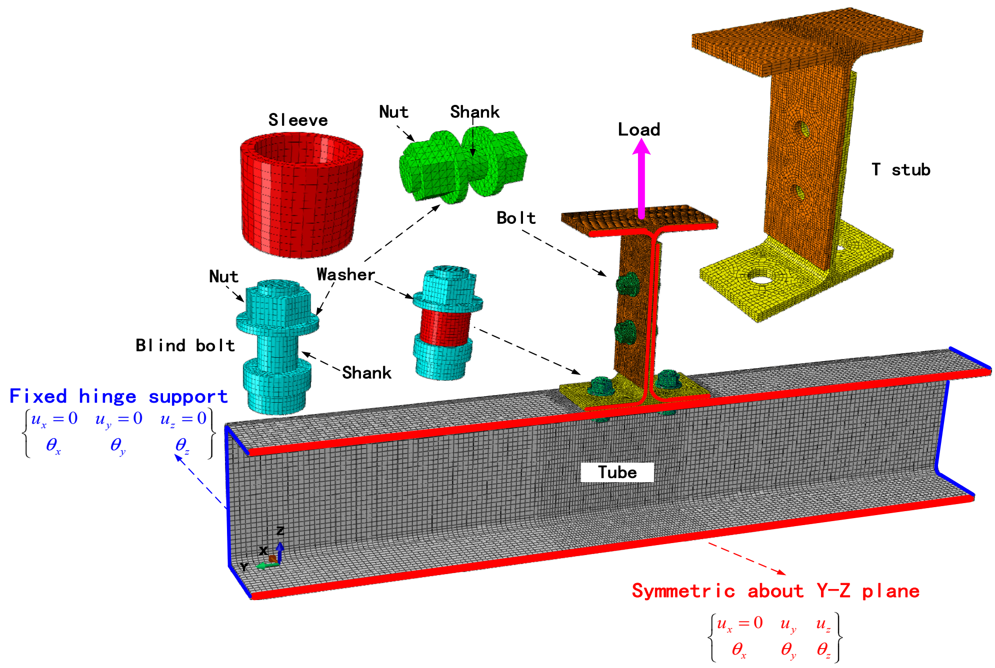

(**b**) Finite element model of TJD-3 and TJD-4

Figure 12. Finite element model.

4.2. Material Models

Two different material models were used for the finite element analysis. Based on the experimental observations, it was evident that various degrees of fractures and damage occurred at the junction between the flange and web of the T-stub, as well as at the bolt holes in the web of the T-stub. Therefore, the constitutive model of Q235 steel considering ductile damage was defined for the T-stub and HSST. High-strength bolts, blind bolts, nuts, sleeves, and washers were modeled using a trilinear material model with isotropic hardening [25].

The T-stub and HSST were made of Q235 steel. Uniaxial tensile tests were conducted on the materials used in the test, with an elastic modulus of E = 206 GPa and a Poisson's ratio μ = 0.3. The engineering stress–strain curve obtained from uniaxial tensile testing was transformed into a true stress–strain curve according to Formulas (1) and (2), as shown in Figure 13. The ductile damage model in ABAQUS and the element removal technique were employed to account for the failure modes. Based on the behavior of the tensile specimens and the principle of metal damage model described in Reference [13], the parameters of the ductile damage initiation criteria and damage evolution laws were analyzed.

$$\varepsilon_{ture} = \ln(1 + \varepsilon_{con}) \quad (1)$$

$$\sigma_{ture} = \sigma_{con}(1 + \varepsilon_{con}) \quad (2)$$

where ε_{com} and ε_{com} are, respectively, the engineering strain and true strain, and σ_{com} and σ_{ture} are, respectively, the engineering stress and true stress.

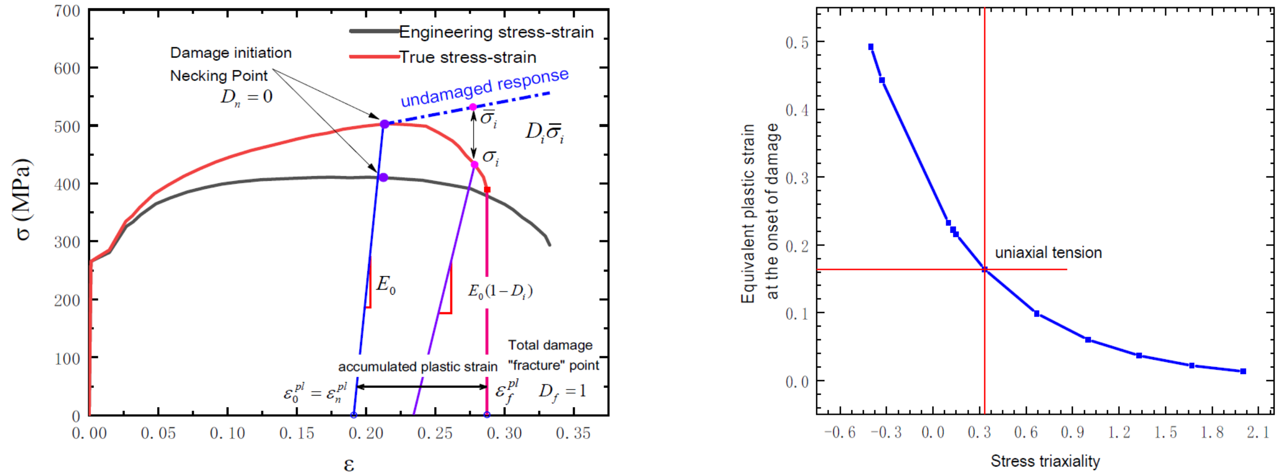

(**a**) Stress–strain curve (**b**) Equivalent plastic stress–strain triaxial curve

Figure 13. Plasticity and ductile damage parameters for steel materials.

The damage fracture criterion, that is, a functional relationship between the equivalent plastic strain and the stress triaxiality, should be formulated, and the equivalent plastic strain is $\bar{\varepsilon}_0^{pl}$ at the onset of damage in the function of stress triaxiality θ. Corresponding to the standard tensile test, the equivalent plastic strain at the initiation of damage can be defined as $\bar{\varepsilon}_0^{pl} = \varepsilon_0^{pl} = \varepsilon_n^{pl}$, where ε_0^{pl} is the plastic strain obtained from the experimental results of standard tensile tests, and ε_n^{pl} is defined in Figure 13a as the uniaxial true plastic strain at the onset of the necking point. The function describing the relationship between the equivalent plastic strain at the initiation of damage and stress triaxiality was established based on both experimental data and theoretical insights provided by various researchers. Trattnig et al. [26] carried out a series of experiments on austenitic steels, varying the triaxiality conditions. Drawing from their experimental findings, they formulated an exponential relationship between the equivalent plastic strain at fracture ($\bar{\varepsilon}_f^{pl}$) and triaxiality. This relationship is expressed through Equation (3), which is characterized by the material constants α and β. A similar fracture boundary was also theoretically derived by Rice and Tracey [27], establishing an exponential connection between void growth rate and triaxiality.

$$\bar{\varepsilon}_f^{pl} = \alpha \cdot \exp(-\beta \cdot \theta) \quad (3)$$

The same expression formulated for the uniaxial strain state, according to the calculation Formula (3), can be used to derive the ratio of the equivalent plastic strain at fracture to the uniaxial strain at fracture, given by $\bar{\varepsilon}_f^{pl}/\varepsilon_f^{pl}$ in Equation (4).

$$\bar{\varepsilon}_f^{pl}/\varepsilon_f^{pl} = \exp[-\beta(\theta - 1/3)] \tag{4}$$

The material parameter β = 1.5 is employed, as suggested by Rice and Tracey [28]. Ultimately, $\varepsilon_0^{pl} = \varepsilon_n^{pl}$ is utilized as the criterion for damage initiation, as per Equation (5). The criteria are illustrated in Figure 13b.

$$\bar{\varepsilon}_0^{pl}(\theta) = \varepsilon_n^{pl} \cdot \exp[-1.5 \cdot (\theta - 1/3)] \tag{5}$$

Once the criteria for initiating damage are established, the plasticity curves and damage evolution laws required for integration into the ABAQUS material models are derived from experimental data obtained through standard tensile tests.

In order to facilitate the subsequent analysis, the identification of key characteristic points within both nominal and true stress–strain curves becomes essential. These critical points include (1) p: the onset of plasticity, (2) n: the initiation of necking, signifying the initiation of damage, (3) r: the point of rupture, indicating a critical state of damage, and (4) f: the fracture point, representing total damage. Illustrations of these pivotal points are provided in Figure 12a, specifically for the material utilized in bolt applications.

$$D_i = \begin{cases} (1 - \sigma_i/\overline{\sigma}_i)\alpha_D, n \le i \le r \\ 1, i = f \end{cases} \tag{6}$$

The damage variable is derived as the dimensionless difference between the material's undamaged response defined by Equation (6) and its damaged response. Figure 12a illustrates that at the rapture point denoted as $\boldsymbol{r}$, the material undergoes a critical level of damage $\boldsymbol{D_i}$, immediately followed by the fracture point **f**, where stiffness experiences complete degradation. This behavior has also been noted by Lamaitre [29], who defines the critical damage value for most steels as $\boldsymbol{D_i}$, ranging between 0.2 and 0.5. Bonora et al. [28] also made observations indicating that the actual critical damage values for steel materials tend to be higher, falling within the range of 0.55 to 0.65. To account for this, an introduced factor termed the damage eccentricity factor (α_D) was incorporated into Equation (6). The values of α_D varied between 1.5 and 1.7 for the distinct types of steels employed in this study.

According to the test phenomenon, no failure occurred in the bolts. For this analysis, bolts, nuts, sleeves, and washers were characterized using a three-segment linear material isotropic kinematic hardening ideal elastoplastic model. The materials were determined according to a previous specification [30], where the Young's modulus was 206 GPa, the yield strength and tensile strength were 900 MPa and 1040 MPa, respectively, the plastic strain was 0.1, and the Poisson's ratio was 0.3.

4.3. Validation of Numerical Results

The force–displacement relationship curve of each specimen calculated using the finite element method was compared with that of the test, as shown in Figure 14. It can be seen from the figure that the curves are in good agreement, indicating that the material model and boundary conditions defined by the finite element model are consistent with the actual conditions.

Figure 15 shows a comparison of the deformation characteristics of all specimens. It can be seen that during the elastic–plastic stage, the deformation of the T-stub in all specimens was mainly caused by the bending deformation of the flange. With a progressively increasing load, the occurrence of fracture in the T-stub becomes evident, gradually evolving into fracture failure in tandem with the development of plastic damage. TJD-1 and TJD-2 exhibited fracture failure at the juncture between the T-stub's web and flange. In the case of the specimen TJD-1, the fracture in the T-stub occurred when the stress reached 496 N/mm^2. For the specimen TJD-2, the fracture in the T-stub occurred at a stress level of 502 N/mm^2. The webs of the T-stubs in the specimens TJD-3 and TJD-4 were equipped with connecting bolts. Under the action of the load, the fracture failure of specimen TJD-3 still occurred at the junction of the web and flange, and the fracture occurred when the stress reached 498 N/mm^2. As for the specimen TJD-4, the squeezing effect of the bolt holes in the web was obvious. The stress value at this point was greater than that at other places, and when the stress value reached 518 N/mm^2, the cracks in the T-stub's web gradually extended along the horizontal direction of the bolt holes.

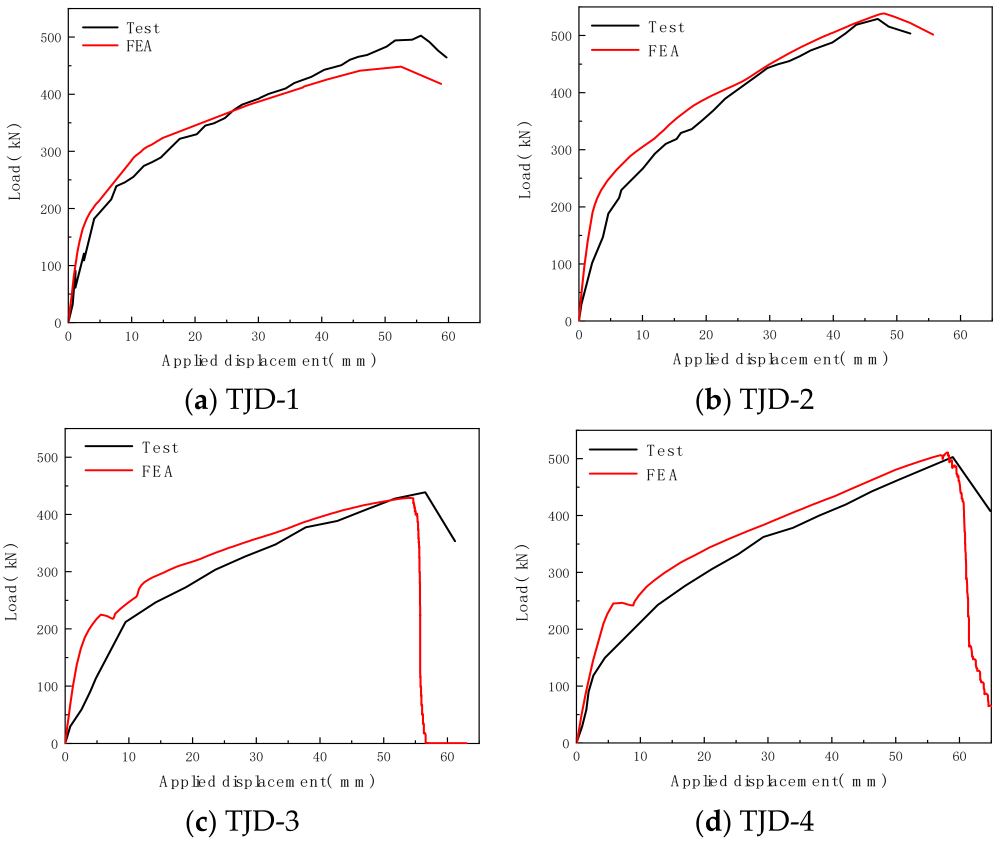

Figure 14. Comparison of test and FEM simulation curves.

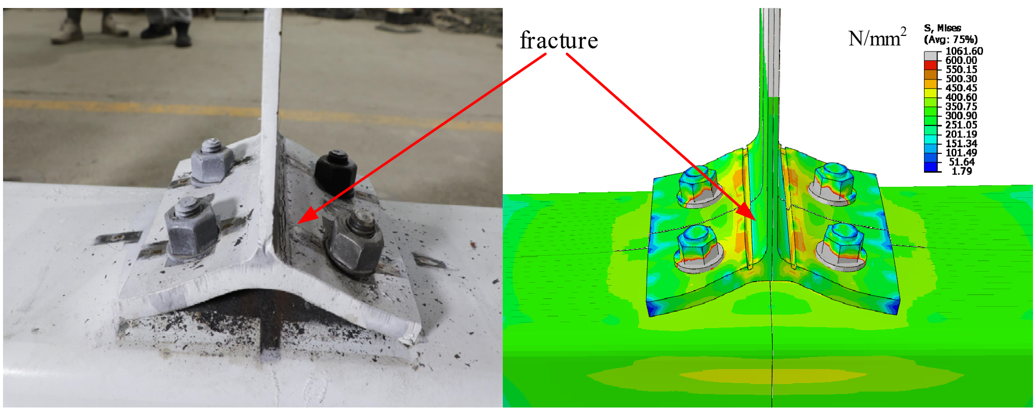

(**a**) TJD-1

Figure 15. *Cont.*

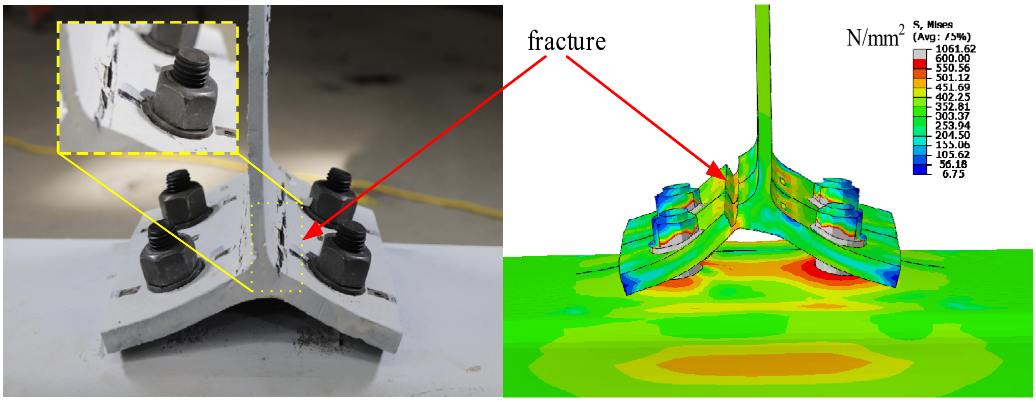

(**b**) TJD-2

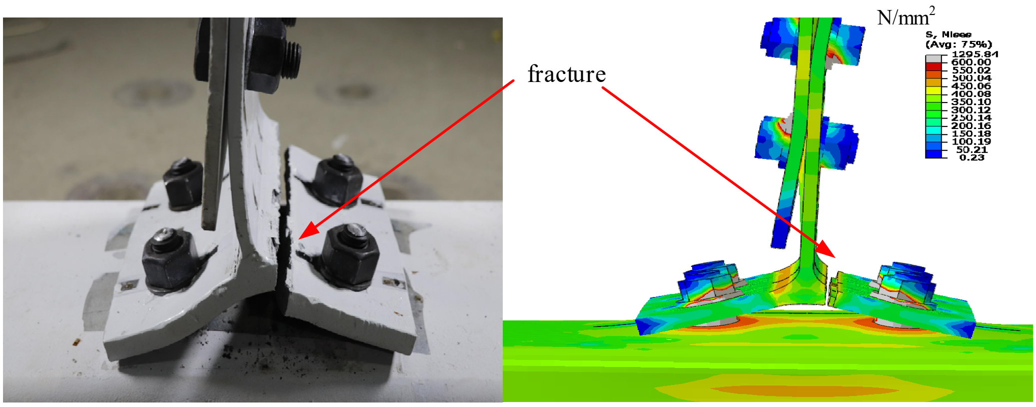

(**c**) TJD-3

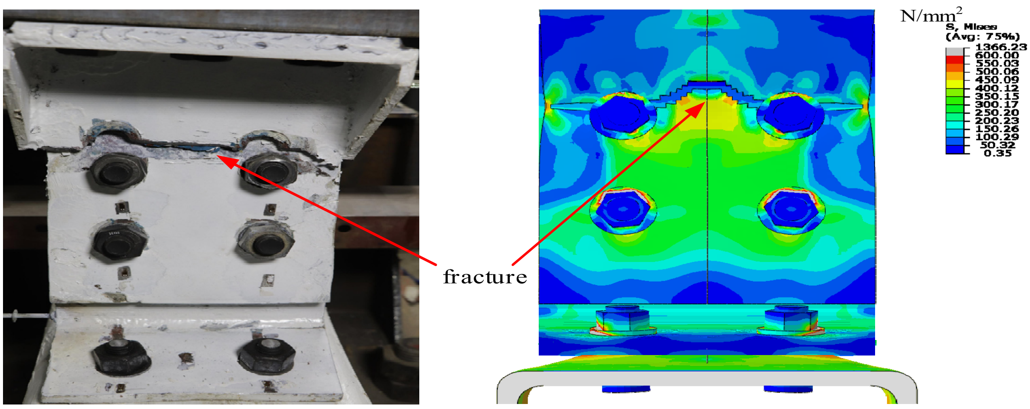

(**d**) TJD-4

Figure 15. Comparison of deformation characteristics.

5. Damage Process Analysis

The concept of performance-based seismic design (PBSD) helps designers to deliberately manage structural damage within acceptable limits during earthquakes of varying intensities. This approach requires a precise evaluation of seismic damage, thereby highlighting the significance of damage models in establishing a connection between structural performance and the resulting damage levels. The damage models combining deformation ductility and dissipated energy appear to be more reasonable. One of the best-known and most widely-used cumulative damage models is the Park–Ang model. Therefore, this study adopts the modified model of Kunnath [31], which considers the cumulative damage correction of residual deformation, to calculate the damage index of the connection specimens. The expression of the damage index, DI, is as follows:

$$DI = (1-\beta)\frac{\delta_m - \delta_y}{\delta_u - \delta_y} + \beta\frac{\int dE}{f_y \delta_u} \quad \delta_m = \begin{cases} \delta_y, & \delta_m \leq \delta_y \\ \delta_m, & \delta_m > \delta_y \end{cases} \tag{7}$$

where δ_m represents the deformation corresponding to each loading stage under monotonic loading, δ_u is the deformation at the ultimate state under monotonic loading, f_y is the yield strength of the steel material, dE is the energy dissipated due to plastic deformation, β is a non-negative combination coefficient, and for steel structures, β is assigned a value of 0.025 [32].

The calculated damage index can be used to estimate the structural damage state, and the damage index has been paid attention by FEMA and other standards because of its simple calculation and clear physical concept [33]. As the basis for determining the FEMA performance level, the correlation between the plastic ductility index and other damage indicators will be of great significance, which provides the consistency and reliability of the FEMA performance level when predicting structural damage under seismic excitation. This index was proposed by Williams [34]. Table 4 shows the damage indices assigned to FEMA performance levels. FEMA 356 specifies the performance levels of the structure in several stages [33]:

1. **Linear limit** (***A-B***): the structure response restricted to the linear limit;
2. **Immediate occupancy** structural performance level (***IO***): the structure will be safe to occupy after the earthquake;
3. **Damage control** structural performance range (***DC***): a damage state between life safety and immediate occupancy performance level;
4. **Life safety** structural performance level (***LS***): structure is damaged, but retains a margin against onset of partial or total collapse;
5. **Limited safety** structural performance range (***LSR***): a damage state between collapse prevention and life safety performance level;
6. **Collapse prevention** structural performance level (***CP***): the structure continues to support gravity loads, but retains no margin against collapse;
7. **Collapsed** (***C***).

Table 4. Damage indices assigned to FEMA performance levels.

FEMA Performance Level	***A-B***	***IO***	***DC***	***LS***	***LSR***	***CP***	***C***
FEMA Damage Index	0	0.17	0.33	0.50	0.67	0.83	1

Using Formula (1), the damage index of all connections was calculated, and the damage development status of all connections was evaluated based on the calculation results. The evaluation results are shown in Figure 16. As observed from Figure 16, when the loading displacement reached the yield displacement, the damage indices of TJD-1, TJD-2, TJD-3, and TJD-4 were very low, each being less than 0.17, indicating that the structure had only slight deformation and no damage occurred. As the yield displacement of TJD-1 was the lowest among all specimens, this indicates that it was prone to experiencing larger deformations under tension, so the IO range of TJD-1 was the widest. Similarly, TJD-1 had the highest ductility coefficient among all specimens, resulting in the TJD-1 damage index range being the broadest and the connection being the most susceptible to damage. Comparing Figure 16a,b, as well as Figure 16c,d, it can be seen that in increasing the thickness of the T-stub's flange, the deformation capacity of the connection decreased. Taking into account the influence of shear-loaded connecting bolts in the T-stub's web on the damage characteristics of the connection, and comparing Figure 16a,c, as well as Figure 16b,d, it is found that the shear-loaded connecting bolts share the internal forces of the T-stub, resulting in a decrease in the internal force transmitted to the flange, so the deformation of the flange is reduced, narrowing the range of the damage index of the connection.

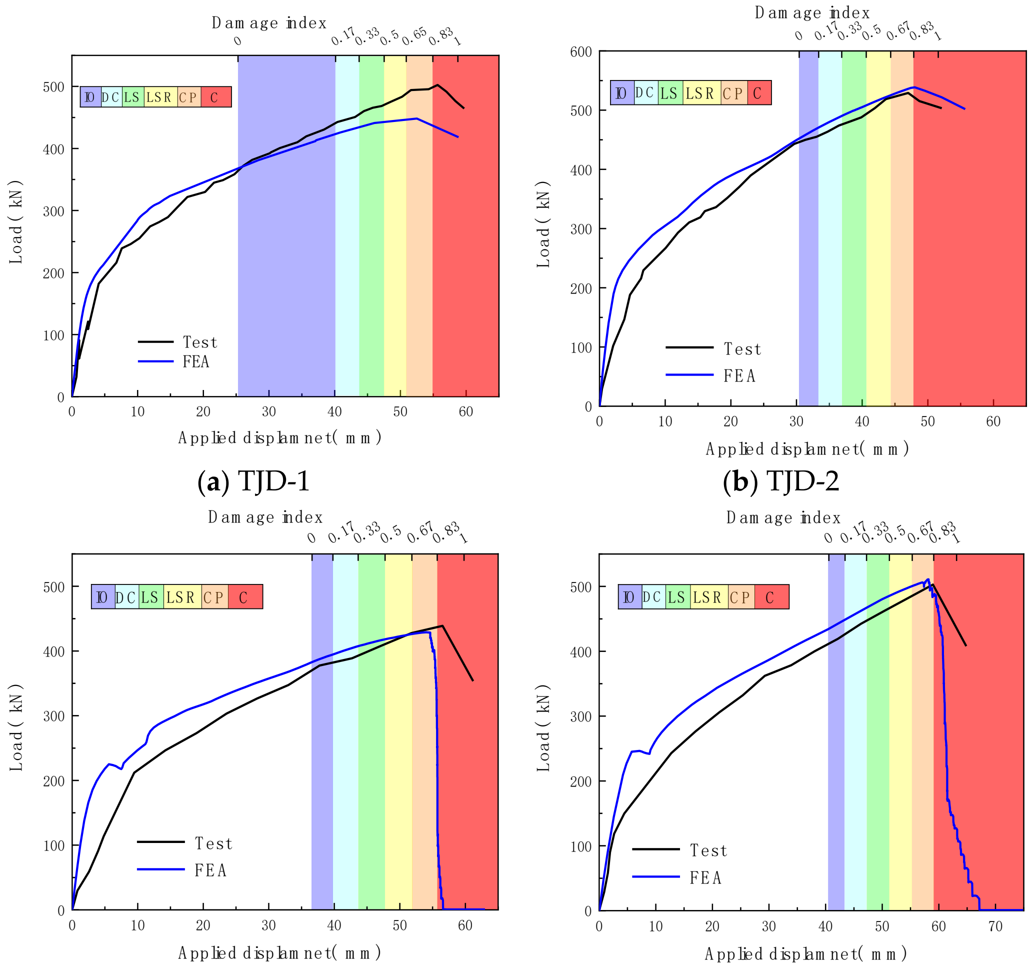

(**a**) TJD-1 (**b**) TJD-2

(**c**) TJD-3 (**d**) TJD-4

Figure 16. Damage index distribution of connection.

As the load continued to increase, each specimen progressively entered the stages of damage control (***DC***), life safety (***LS***), limited safety (***LSR***), and collapse prevention (***CP***). From Figure 16, it can be observed that the damage index ranges within each damage stage are quite similar. Combining the experimental observations and finite element analysis, it is concluded that the primary reasons for the progression of connection damage are the bending deformation of the T-stub's flange and its fracture. The failure behavior of TJD-3 and TJD-4, which had shear-loaded connecting bolts on the T-stub's web, not only involves bending deformation of the flange but also the fracture of the web. It can be seen from Figure 16c,d that the force–displacement curves of TJD-3 and TJD-4 exhibited a significantly faster decrease in load-bearing capacity during the failure stage compared with TJD-1 and TJD-2. The red area in Figure 15 represents the complete failure of all of the connections, indicating that all of the test specimens completely failed and were unable to continue to withstand the tensile load. Upon analysis, it is evident that the force–displacement curves for all test specimens enter Stage C after exceeding the ultimate load. This behavior aligns with the experimental observations, confirming that the calculation method for the damage index is consistent with the damage ranges prescribed by FEMA.

6. Conclusions

In this study, a T-stub connected to a hollow section column using blind bolts was taken as the research object, and the mechanical properties and damage characteristics were studied using tests and the finite element method. The main conclusions are as follows:

1. There are three main failure modes of this connection: the out-of-plane plastic deformation of the wall of HSST and the bending fracture failure of the T-stub's flange. When the T-stub's web contains shear-loaded connecting bolts, it will cause the fracture of the web.
2. Increasing the thickness of the T-stub can improve the tensile-bearing capacity of the connection. Under the condition that the wall thickness of the hollow square steel tube is not changed, the initial tensile stiffness is not increased significantly, which indicates that the out-of-plane deformation and tensile force of the wall of the hollow square steel tube have a dominant effect on the initial tensile stiffness of the connection under the yielding state.
3. For a connection with a T-stub containing shear-loaded connecting bolts, the tensile force of the web is transmitted through the shear-loaded connecting bolts to the web of the T-stub, causing the bolt holes on the web to be squeezed. As the load gradually increases with the increase in the squeezing effect, the plastic deformation generated by the bolt hole reduces the force transmission effect, which is the main reason for the decrease in the mechanical performance of the connection.
4. Finite element analysis considering ductile damage can effectively simulate the plastic deformation process and failure mode of T-stubs connected to hollow section columns.
5. The damage index model adopted in this study can accurately reflect the damage characteristics of the T-stub–hollow-section column connections and can accurately reflect the seven damage stages specified by FEMA. The damage indices are all smaller than 0.17 before the connections yield, and are beyond 0.83 when the connections enter the failure stage. The quantitative assessment conducted here established a correlation between damage states and damage characteristics, thereby enabling a quantitative evaluation of this specific type of connection's damage.

Author Contributions: Conceptualization, X.W. and X.B.; methodology, X.B.; software, Z.W.; validation, S.X.; formal analysis, X.L.; writing—original draft preparation, X.B.; writing—review and editing, S.X.; supervision, X.W.; project administration, X.W.; funding acquisition, X.B., Z.W. and X.L. All authors have read and agreed to the published version of the manuscript.

Funding: This research was funded by the Henan Province University Youth Key Teacher Training Project (grant number: 2020GGJS244) and the Key Scientific Research Project Plan of Henan Province University (grant number: 23B560009). This work was also supported by the Henan Provincial Department of Science and Technology Research Project (grant number: 222102320114).

Data Availability Statement: The testing and analysis data used to support the findings in this study are included within the article.

Conflicts of Interest: The authors declare no conflict of interest.

References

1. Ferdous, W.; Bai, Y.; Ngo, T.D.; Manalo, A.; Mendis, P. New advancements, challenges and opportunities of multi-storey modular buildings–A state-of-the-art review. *Eng. Struct.* **2019**, *183*, 883–893. [CrossRef]
2. Lawson, R.M.; Ogden, R.G. 'Hybrid' light steel panel and modular systems. *Thin-Walled Struct.* **2008**, *46*, 720–730. [CrossRef]
3. Swanson, J.A.; Leon, R.T. Bolted Steel Connections: Tests on T-Stub Components. *J. Struct. Eng.* **2000**, *126*, 50–56. [CrossRef]
4. Bayat, M.; Zahrai, S.M. Seismic performance of mid-rise steel frames with semi-rigid connections having different moment capacity. *Steel Compos. Struct.* **2017**, *25*, 1–17.
5. Piluso, V.; Rizzano, G. Experimental analysis and modelling of bolted T-stubs under cyclic loads. *J. Constr. Steel Res.* **2008**, *64*, 655–669. [CrossRef]
6. Bruneau, M. Performance of steel bridges during the 1995 Hyogoken–Nanbu (Kobe, Japan) earthquake—A North American perspective. *Eng. Struct.* **1998**, *20*, 1063–1078. [CrossRef]

7. Kılıç, M.; Maali, M.S.; Maali, M.; Aydın, A.C. Experimental and numerical investigation of semi-rigid behavior top and seat T-Section connections with different triangular designed stiffener thicknesses. *Eng. Struct.* **2023**, *289*, 116216. [CrossRef]
8. Liu, X.C.; Pu, S.H.; Zhang, A.L.; Zhan, X.X. Performance analysis and design of bolted connections in modularized prefabricated steel structures. *J. Constr. Steel Res.* **2017**, *133*, 360–373. [CrossRef]
9. Liu, X.C.; He, X.N.; Wang, H.X.; Yang, Z.W.; Pu, S.H.; Zhang, A. Bending-shear performance of column-to-column bolted-flange connections in prefabricated multi-high-rise steel structures. *J. Constr. Steel Res.* **2018**, *145*, 28–48. [CrossRef]
10. Wang, W.; Li, L.; Chen, D. Progressive collapse behaviour of endplate connections to cold-formed tubular column with novel Slip-Critical Blind Bolts. *Thin-Walled Struct.* **2018**, *131*, 404–416. [CrossRef]
11. Tizani, W.; Al-Mughairi, A.; Owen, J.S.; Pitrakkos, T. Rotational stiffness of a blind-bolted connection to concrete-filled tubes using modified Hollo-bolt. *J. Constr. Steel Res.* **2013**, *80*, 317–331. [CrossRef]
12. Wang, P.; Sun, L.; Liu, M.; Zhang, B.; Hu, X.; Yu, J. Experimental studies on thread-fixed one-side bolted connection of beam to hollow square steel tube under static bending moment. *Eng. Struct.* **2020**, *214*, 110655. [CrossRef]
13. Wang, P.; Sun, L.; Zhang, B.; Yang, X.; Liu, F.; Han, Z. Experimental studies on T-stub to hollow section column connection bolted by T-head square-neck one-side bolts under tension. *J. Constr. Steel Res.* **2021**, *178*, 106493. [CrossRef]
14. *EN 1993-1-8*; Design of Steel Structures—Part 1–8: Design of Joints. European Committer for Standardization: Brussel, Belgium, 2005.
15. Guo, H.; Liang, G.; Li, Y.; Liu, Y. Q690 high strength steel T-stub tensile behavior: Experimental research and theoretical analysis. *J. Constr. Steel Res.* **2017**, *139*, 473–483. [CrossRef]
16. Liang, G.; Guo, H.; Liu, Y.; Yang, D.; Li, S. A comparative study on tensile behavior of welded T-stub joints using Q345 normal steel and Q690 high strength steel under bolt preloading cases. *Thin-Walled Struct.* **2019**, *137*, 271–283. [CrossRef]
17. Sun, F.F.; Xue, X.Y.; Xiao, Y.; Le, Y.M.; Li, G. Effect of welding and complex loads on the high-strength steel T-stub connection. *J. Constr. Steel Res.* **2018**, *150*, 76–86. [CrossRef]
18. Yapici, O.; Theofanous, M.; Afshan, S.; Yuan, H.; Dirar, S. Numerical modelling of stainless steel bolted T-stubs in tension. *Thin-Walled Struct.* **2022**, *177*, 109432. [CrossRef]
19. Yapici, O.; Theofanous, M.; Yuan, H.; Dirar, S.; Afshan, S. Numerical simulation and design of ferritic stainless steel bolted T-stubs in tension. *J. Constr. Steel Res.* **2022**, *198*, 107555. [CrossRef]
20. Wang, P.; Sun, L.; Xia, C.; Gu, H.; Liu, Y.; Liu, M.; Liu, F. Cyclic behavior of T-stub connection to hollow section steel column using TSOBs. *J. Constr. Steel Res.* **2021**, *185*, 106874. [CrossRef]
21. Wang, P.; Wulan, T.; Liu, M.; Qu, H.; You, Y. Shear behavior of lap connection using one-side bolts. *Eng. Struct.* **2019**, *186*, 64–85. [CrossRef]
22. Sun, L.; Liu, M.; Liu, Y.; Wang, P.; Zhao, H.; Sun, J.; Shang, Y. Studies on T-shaped one-side bolted connection to hollow section column under bending. *J. Constr. Steel Res.* **2020**, *175*, 106359. [CrossRef]
23. Yu, H.; Burgess, I.W.; Davison, J.B.; Plank, R.J. Numerical simulation of bolted steel connections in fire using explicit dynamic analysis. *J. Constr. Steel Res.* **2008**, *64*, 515–525. [CrossRef]
24. Irvani, M.; Ezati, H.; Khafajeh, R.; Jaari, V.R.K. Numerically study on the seismic response of partially restrained moment connection with structural fuse T-stub for European sections. *Structures* **2022**, *35*, 82–105. [CrossRef]
25. D'Aniello, M.; Cassiano, D.; Landolfo, R. Simplified criteria for finite element modelling of European preloadable bolts. *Steel Compos. Struct.* **2017**, *24*, 643–658.
26. Trattnig, G.; Antretter, T.; Pippan, R. Fracture of austenitic steel subject to a wide range of stress triaxiality ratios and crack deformation modes. *Eng. Fract. Mech.* **2008**, *75*, 223–235. [CrossRef]
27. Rice, J.R.; Tracey, D.M. On the ductile enlargement of voids in triaxial stress fields. *J. Mech. Phys. Solids* **1969**, *17*, 201–217. [CrossRef]
28. Bonora, N.; Ruggiero, A.; Esposito, L.; Gentile, D. CDM modeling of ductile failure in ferritic steels: Assessment of the geometry transferability of model parameters. *Int. J. Plast.* **2006**, *22*, 2015–2047. [CrossRef]
29. Lemaitre, J. A Continuous Damage Mechanics Model for Ductile Fracture. *J. Eng. Mater. Technol.* **1985**, *107*, 83–90. [CrossRef]
30. *GB/T 1231-2006*; Specifications of High Strength Bolts with Large Hexagon Head, Large Hexagon Nuts, Plain Washers for Steel Structures. Standards Press of China: Beijing, China, 2006.
31. Kunnath, S.K.; Reinhorn, A.M.; Park, Y.J.; Kunnath, A.M.S.K.; Member, A.A. Analytical Modeling of Inelastic Seismic Response of R/C Structures. *J. Struct. Eng.* **1990**, *116*, 996–1017. [CrossRef]
32. Park, Y.J.; Ang, A.H.-S.; Wen, Y.K. Damage-Limiting Aseismic Design of Buildings. *Earthq. Spectra* **1987**, *3*, 1–26. [CrossRef]
33. *FEMA-356*; Prestandard and Commentary for the Seismic Rehabilitation of Buildings. Federal Emergency Management Agency: Washington, DC, USA, 2000.
34. Williams, M.S.; Sexsmith, R.G. Seismic damage indices for concrete structures: A state-of-the-art review. *Earthq. Spectra* **1995**, *11*, 319–349. [CrossRef]